Plasma-Enhanced Atomic Layer Deposition of Nanostructured Gold Near Room Temperature

Michiel Van Daele,[†] Matthew B. E. Griffiths,[‡] Ali Raza,[§,||] Matthias M. Minjauw,[†] Eduardo Solano,[⊥] Ji-Yu Feng,[†] Ranjith K. Ramachandran,[†] Stéphane Clemmen,[§,||,#] Roel Baets,[§,||] Seán T. Barry,[‡] Christophe Detavernier,[†] and Jolien Dendooven*,[†]

[†]Department of Solid State Sciences, COCOON Group, Ghent University, 9000 Gent, Belgium
[||]Center for Nano- and Biophotonics, Ghent University, 9052 Gent, Belgium
[‡]Department of Chemistry, Carleton University, K1S 5B6 Ottawa, Canada
[§]Photonics Research Group, INTEC Department, Ghent University—IMEC, 9052 Gent, Belgium
[⊥]ALBA Synchrotron Light Source, NCD-SWEET Beamline, 08290 Cerdanyola del Valles, Spain
[#]Laboratoire d'Information Quantique, Université Libre de Bruxelles, 1050 Bruxelles, Belgium

Ⓢ Supporting Information

ABSTRACT: A plasma-enhanced atomic layer deposition (PE-ALD) process to deposit metallic gold is reported, using the previously reported $Me_3Au(PMe_3)$ precursor with H_2 plasma as the reactant. The process has a deposition window from 50 to 120 °C with a growth rate of 0.030 ± 0.002 nm per cycle on gold seed layers, and it shows saturating behavior for both the precursor and reactant exposure. X-ray photoelectron spectroscopy measurements show that the gold films deposited at 120 °C are of higher purity than the previously reported ones (<1 at. % carbon and oxygen impurities and <0.1 at. % phosphorous). A low resistivity value was obtained (5.9 ± 0.3 $\mu\Omega$ cm), and X-ray diffraction measurements confirm that films deposited at 50 and 120 °C are polycrystalline. The process forms gold nanoparticles on oxide surfaces, which coalesce into wormlike nanostructures during deposition. Nanostructures grown at 120 °C are evaluated as substrates for free-space surface-enhanced Raman spectroscopy (SERS) and exhibit an excellent enhancement factor that is without optimization, only one order of magnitude weaker than state-of-the-art gold nanodome substrates. The reported gold PE-ALD process therefore offers a deposition method to create SERS substrates that are template-free and does not require lithography. Using this process, it is possible to deposit nanostructured gold layers at low temperatures on complex three-dimensional (3D) substrates, opening up opportunities for the application of gold ALD in flexible electronics, heterogeneous catalysis, or the preparation of 3D SERS substrates.

KEYWORDS: atomic layer deposition, nanoparticles, plasmonics, SERS, gold metal

1. INTRODUCTION

Gold as a bulk material has found a widespread use in jewelry, coinage, and decorative pieces because of its unreactive nature. However, nanoparticulate gold has very interesting and useful catalytic properties and has attracted significant interest for heterogeneous catalysis.[1−3] The use of nanoparticulate gold for heterogeneous catalysis remains a growing research field.

Suspended gold nanoparticles (or colloidal gold) are often used for their inherent optical properties (e.g., colloidal gold in ruby glass).[4] The optical properties arise because of the localized surface plasmon resonances (LSPR) that develop at the metal surface. The LSPR can create electromagnetic hotspots between metallic structures, and these hotspots can cause enormous enhancement of a Raman signal.[5,6] The most used materials for surface-enhanced Raman spectroscopy (SERS) are silver and gold because of their surface plasmon properties. A drawback of using silver in SERS substrates is that it easily tarnishes while this is not the case for gold. In general, highly ordered nanostructures are required for solid-state SERS substrates. By tuning the properties of the nanostructures on the SERS substrate, it is possible to achieve single molecule detection. A major fallback in present SERS substrates is that fabrication often involves several processing and deposition steps, making the production process expensive, complex, and difficult to implement simply and on a large scale.

Atomic layer deposition (ALD) offers precise control over the amount of material deposited on a substrate because of the alternating exposure of the substrate to the precursor and reactant gases. These gas phase species undergo self-limiting reactions with the substrate, which allows conformal films to be deposited on planar and complex 3D substrates. This makes ALD an extremely useful deposition method for gold nanoparticles on substrates that are challenging for other deposition methods (e.g., physical vapor deposition or solution-based methods).

Gold metal is extremely challenging to be deposited by ALD: only two gold ALD processes have been reported, although many chemical vapor deposition (CVD) precursors exist to deposit gold.[7−11] However, finding precursors that are suitable for ALD has proven to be quite difficult because they need to be thermally stable, volatile, have decent surface-limited reactions, and saturation behavior.[12] Another aspect is the need for suitable reducing agents for the precursor. The first gold ALD process was reported by Griffiths, Pallister, Mandia, and Barry.[13] This plasma-enhanced ALD (PE-ALD) process consists of three steps: the surface is first exposed to trimethylphosphinotrimethylgold(III) ($Me_3Au(PMe_3)$), followed by oxygen plasma exposure, and finally, a water vapor exposure. Deposition of metallic gold was reported at a deposition temperature of 120 °C with a growth rate of 0.05 nm per cycle. The deposited films had some impurities, 6.7 at. % carbon, and 1.8 at. % oxygen. The second gold ALD process was reported by Mäkelä, Hatanpää, Mizohata, Räisänen, Ritala, and Leskelä.[14] This process employs $Me_2Au(S_2CNEt_2)$ as the gold precursor and ozone as the reactant. Deposition between 120 and 180 °C was reported, with self-limiting growth at a substrate temperature of 180 °C. A relatively high growth rate of 0.09 nm per cycle was achieved. These films showed low resistivity (4.6−16 $\mu\Omega$ cm) with some impurities 2.9 at. % oxygen, 0.9 at. % hydrogen, 0.2 at. % carbon, and 0.2 at. % nitrogen.

In this work, we report a gold PE-ALD process using the existing $Me_3Au(PMe_3)$ gold precursor in combination with H_2 plasma as the reactant. Compared to the other two reported gold ALD processes, this process showed self-limiting behavior at temperatures as low as 50 °C. This makes it possible to use the reported process in applications that utilize temperature-sensitive substrates, such as flexible electronics.[15−17] Another advantage over the previously reported gold ALD processes is the use of a reducing coreactant (H_2 plasma) instead of oxidizing chemistry (O_2 plasma or O_3), hence avoiding the oxidation of the underlying substrate surface. The deposited films have an intrinsic nanoparticle structure, interesting for heterogeneous catalysis and plasmonic applications. It is shown that the films grown at 120 °C exhibit excellent SERS properties, revealing that the presented PE-ALD process offers a relatively easy route toward large-scale SERS substrates with potential applications in sensing devices.[18,19]

2. EXPERIMENTAL SECTION

All ALD processes were carried out in a home-built pump-type ALD reactor with a base pressure of 2×10^{-6} mbar.[20] Computer-controlled pneumatic valves and manually adjustable needle valves were used to control the dose of the precursor vapor and reactant gas. The $Me_3Au(PMe_3)$ precursor (≥95% purity) was synthesized using the method described in the Supporting Information of the article by Griffiths, Pallister, Mandia, and Barry.[13] The precursor was kept in a glass container which was heated to 50 °C during deposition processes, and the delivery line was heated to 55 °C. Argon was used

as the carrier gas during all deposition processes. The flow of the carrier gas was adjusted to reach 6×10^{-3} mbar in the chamber when pulsing. The precursor exposure during the ALD processes were carried out by injecting the $Me_3Au(PMe_3)$ vapor after closing the gate valve between the turbomolecular pump and the reactor chamber. By varying the injection time, the pressure during the pulse varied between 6×10^{-3} and 5 mbar. After injection, the precursor vapor was kept in the ALD chamber for an additional 5 s before evacuating the chamber. H_2 plasma (20% H_2 in argon) was used as the reactant for all deposition processes. Previously, some of the authors reported that using H_2 gas or H_2 plasma as the reactant in combination with the $Me_3Au(PMe_3)$ precursor does not lead to gold deposition. However, they used a low concentration of H_2 gas in comparison with the 20% that was used in this work, possibly explaining this different result. H_2 gas was introduced through the plasma column mounted on top of the chamber, and the flow of H_2 gas was limited by a needle valve to obtain a chamber pressure of 6×10^{-3} mbar during all deposition processes. A 13.56 MHz radio frequency generator (Advanced Energy, model CESAR 136) and a matching network were used to generate an inductively coupled plasma in the plasma column. For all the experiments, a plasma power of 200 W was used and the impedance matching parameters were adjusted to minimize the reflected power. H_2 plasma exposure of 10 s was used before each deposition. The used substrates were pieces of p-type silicon (100) with native or thermal silicon oxide or 10 nm sputtered gold films on p-type silicon (100). The samples were mounted directly on a heated copper block. The temperature of the copper block was adjusted with a proportional-integral-derivative (PID) controller. The chamber walls were heated to 100 °C for all experiments, except for the experiments to determine the temperature window, for these experiments, the chamber walls were heated to 50 °C. This was necessary to allow the copper block to be heated at temperatures below 80 °C because it was not possible to use active cooling of the copper block.

Several ex situ measurement techniques were used to determine the physical properties of the deposited Au films. X-ray diffraction (XRD) patterns were acquired to determine the crystallinity of the deposited films. XRD measurements were done on a diffractometer (Bruker D8) equipped with a linear detector (Vantec) and a copper X-ray source (Cu Kα radiation). Thickness determination via X-ray reflectivity (XRR) measurements was done on a diffractometer (Bruker D8) equipped with a copper X-ray source (Cu Kα radiation) and a scintillator point detector. However, because the gold ALD films were generally too rough for accurate thickness determination with XRR, X-ray fluorescence (XRF) measurements were used to determine an equivalent film thickness based on a calibration line of sputtered gold films. The obtained standard deviation of the data points from the obtained calibration line was multiplied by 3 and used as an estimated error for each XRF measurement. The XRF measurements were performed using a Mo X-ray source and an XFlash 5010 silicon drift detectorplaced at an angle of 45° and 52° with the sample surface, respectively. An integration time of 200 s was used to acquire the fluorescence spectra. X-ray photoelectron spectroscopy (XPS) was used to determine the chemical composition and binding energy of the deposited films. The XPS measurements were carried out on a Thermo Scientific Theta Probe XPS instrument. The X-rays were generated using a monochromatic Al source (Al Kα). To etch the surface of the deposited films, an Ar^+ ion gun was used at an acceleration voltage of 3 keV and a current of 2 μA. An FEI Quanta 200F instrument was used to perform scanning electron microscopy (SEM) using secondary electrons and energy-dispersive X-ray spectroscopy (EDX) on the deposited films. Four-point probe measurements were performed to determine the resistivity of the deposited gold films. Atomic force microscopy (AFM) measurements were performed on a Bruker Dimension Edge system to determine the surface roughness of the films. AFM was operated in the tapping mode in air.

To study the morphology of the gold nanostructures, ex situ grazing-incidence small-angle X-ray scattering (GISAXS) measurements were performed at the DUBBLE BM26B beamline of the ESRF

synchrotron facility.[21,22] The used energy for the X-ray beam was 12 keV, with an incidence angle of 0.5°. The GISAXS patterns were recorded with a DECTRIS PILATUS3S 1M detector, which consisted of a pixel array of 1043 × 981 (V × H) with a pixel size of 0.172 × 0.172 μm^2, and a sample-detector distance of 4.4 m was used. The samples were measured in a vacuum chamber that had primary slits and a beamstop inside the chamber to reduce scattering. For each GISAXS scattering pattern, an acquisition time of 60 s was used. Standard corrections for primary beam intensity fluctuations, solid angle, polarization, and detector efficiency were applied to the collected images. The IsGISAXS software was used to perform the data analysis of the GISAXS scattering patterns; a distorted-wave Born approximation was used and graded interfaces were assumed for the perturbated state caused by the gold particles. A spheroid particle shape was assumed with a Gaussian distribution for the particle size. The particle arrangement on the surface was modeled using a one-dimensional (1D) paracrystal model, that is, a 1D regular lattice with loss of a long-range order. Initial input parameters for the simulation were obtained from the two-dimensional (2D) scattering data, by taking horizontal (q_y) and vertical (q_z) line profiles at the position of the main scattering peak. The maximum in the horizontal line profile gave information about the mean center-to-center particle distance, while information about the particle height was obtained from the minima and maxima observed in the vertical line profile. The input parameters for the simulation were refined until a decent agreement between the experiment and simulation was obtained.

In order to determine the surface enhancement of the deposited gold films, free-space SERS was performed on several samples. A monolayer of 4-nitrothiophenol (pNTP, Sigma) was used as an analyte that selectively binds to the gold surface using a Au−thiol bond. The SERS samples were thoroughly rinsed with acetone, isopropanol, and deionized water and dried using a N_2 gun. This was followed by a short O_2 plasma exposure, using a PVA-TEPLA GIGAbatch, to remove the remaining contaminants and enhance the binding. The SERS samples were then immersed in 1 mM pNTP solution for 3 h. Finally, the samples were extensively rinsed using ethanol and water to remove unbound pNTP molecules. The number of adsorbed pNTP molecules on the different samples was estimated based on the Au surface area calculations and the reported pNTP density value on Au (see Supporting Information). Raman measurements were performed using a commercial confocal Raman microscope (WITEC Alpha300R+). A 785 nm excitation diode laser (Toptica XTRA II) was used as the free-space pump source. The laser was operated at a low pump power of 0.2 mW to avoid burning or photoreduction of the pNTP molecules. High NA objectives (100×/0.9 EC Epiplan Neofluar; ∞/0) were used to excite the sample and collect the Raman signal. A 100 μm multimode fiber was used as a pinhole connected to a spectrometer equipped with a 600 lpmm grating, and a charge-coupled device camera was cooled to −70 °C (Andor iDus 401 BR-DD). All the Raman spectra were acquired after optimizing the 1339 cm^{-1} peak using an integration time of 1 s.

3. RESULTS AND DISCUSSION

3.1. ALD Properties. The reaction of the $Me_3Au(PMe_3)$ precursor with H_2 plasma was previously reported to not occur.[13] By using a higher vacuum and higher H_2 concentration, this surface reaction was found to proceed in a self-limiting manner. One of the properties of an ALD process is that both reactions show self-limiting behavior. The saturation behavior of $Me_3Au(PMe_3)$ and H_2 plasma exposure was investigated by determining the equivalent growth per cycle (^{eq}GPC, obtained by dividing the equivalent thickness by the number of ALD cycles) on gold seed layers as a function of the respective exposure time (Figure 1). The injection time for the precursor was varied between 1 and 20 s, while the reactant exposure was kept fixed at 20 s. Likewise, the exposure time of the reactant was varied between 1 and 20 s, while the precursor injection time was kept fixed at 20 s. The depositions were
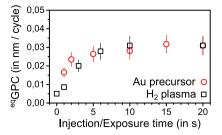

Figure 1. ^{eq}GPC as a function of the injection time and exposure time for the $Me_3Au(PMe_3)$ precursor (○) and H_2 plasma (□), respectively, in the steady growth regime. Depositions were performed on a gold seed layer at a substrate temperature of 100 °C. A total of 100 ALD cycles were performed during each deposition to determine the ^{eq}GPC value. The exposure time of the reactant was kept at 20 s during the saturation experiments of the precursor. The injection time of the precursor was 20 s during the saturation experiments of the reactant. The precursor exposure consisted of an injection time that was varied, followed by a fixed dwell time of 5 s.

performed at a substrate temperature of 100 °C on silicon substrates coated with a thin sputtered gold seed layer (10 nm). The gate valve between the reaction chamber and the turbomolecular pump was closed during the precursor exposure. As mentioned in the experimental section, the exposure time consisted of a variable injection time, followed by a fixed dwell time of 5 s. As a result of the varying injection time, the pressure during the precursor exposure varied between $6 × 10^{-3}$ and 5 mbar. As can be seen in Figure 1, saturation was achieved for $Me_3Au(PMe_3)$ after an injection time of 10 s and after an exposure time of 10 s for H_2 plasma, yielding an ^{eq}GPC of 0.030 ± 0.002 nm per cycle in the steady growth regime.

Pulsing the precursor on a gold substrate without any coreactant resulted in an ^{eq}GPC of 0.005 nm per cycle, implying a minor CVD component for this ALD process. The monolayer of the adsorbed precursor was most likely not perfectly stable and underwent a very slow decomposition to Au(0), forming additional adsorption sites for new precursor molecules. Importantly, there was no deposition when exposing a silicon substrate to only the precursor.

Test depositions under thermal conditions were performed using high pressure H_2 gas (20% H_2 in argon at 25 mbar) instead of H_2 plasma as the reactant. An injection time of 15 s and a dwell time of 5 s were used for the $Me_3Au(PMe_3)$ exposure (i.e., saturating conditions for the PE-ALD process). On silicon substrates, these thermal test depositions did not yield gold deposition in our ALD reactor. However, on gold seed layers some deposition was achieved with an ^{eq}GPC equal to 0.005 nm per cycle, likely originating from the above-mentioned CVD component rather than a chemical reaction with H_2 gas.

The temperature dependence of the ^{eq}GPC for the PE-ALD process with H_2 plasma is shown in Figure 2. The ^{eq}GPC was determined for two precursor injection times, 10 and 20 s, combined with a 15 s H_2 plasma exposure. Decomposition of the precursor occurred for substrate temperatures above 120 °C, as can be concluded from the increase in ^{eq}GPC at 130 and 140 °C. Although the decomposition remained limited for the lower injection time of 10 s, especially at 130 °C, it was severely increased for the 20 s injection time. On the other side of the temperature curve, the growth rate remained constant when lowering the substrate temperature. Moreover, over the
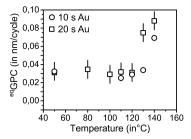
Figure 2. ^{eq}GPC as a function of the substrate temperature for two Me$_3$Au(PMe$_3$) precursor injection time periods, 10 and 20 s with a dwell time of 5 s for both. An exposure time of 15 s was used for H$_2$ plasma. Depositions were performed on a gold seed layer. A total of 100 ALD cycles were performed during each deposition to determine the ^{eq}GPC value. The error bars for the 10 s Au injection time periods were omitted for clarity. Decomposition of the precursor occurs above 120 °C.

whole 50−120 °C temperature range, the ^{eq}GPC achieved with a 10 s precursor injection time was equal to the ^{eq}GPC achieved for the 20 s precursor injection time. This confirms saturation behavior in this temperature range, implying that there is an ALD temperature window from 50 to 120 °C. The lower temperature limit of 50 °C is equal to the temperature of the precursor bottle. Lowering the substrate temperature below the precursor bottle temperature may induce condensation, leading to uncontrolled deposition conditions. On the other hand, decreasing the precursor bottle temperature below 50 °C gave unreliable results in our setup, likely related to limited volatility of the precursor at those temperatures. The 50 °C lower limit of the temperature window makes it possible to deposit gold on temperature-sensitive materials, such as textiles and paper, significantly extending the potential of Au ALD compared to that of the previously reported processes.[13,14] This was verified by depositing a PE-ALD gold film on a piece of a tissue paper at a substrate temperature of 50 °C. EDX measurements were performed on the substrate and showed the presence of gold, as can be seen in Figure 3. This shows that the reported process can be used to deposit gold films on temperature-sensitive substrates, which have potential applications for flexible and wearable electronic devices.[15,16]

The growth of the process on silicon substrates, with native oxide and thermal oxide, was investigated up to an equivalent
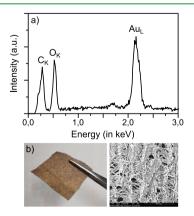

Figure 3. (a) EDX spectrum of a gold-coated piece of tissue paper. The deposition was performed at a substrate temperature of 50 °C. (b) Picture of the measured piece of the paper and (c) a SEM image of the sample.

thickness of 65.6 nm. The PE-ALD depositions were carried out at a substrate temperature of 120 °C, using saturating exposure times. The thickness of the depositions as a function of the number of ALD cycles is shown in Figure S1a, while the ^{eq}GPC is plotted as a function of the number of ALD cycles in Figure S1b. This latter plot reveals a constant ^{eq}GPC when 400 cycles or more are applied. A similar value of 0.029 ± 0.003 nm per cycle was obtained on both the native and the thermal SiO$_2$ surface, which is in agreement with the ^{eq}GPC on gold seed layers. The deviation of the ^{eq}GPC below 400 cycles is an indicative of a nucleation-controlled growth mechanism on a silicon oxide surface. This is not that surprising because metal ALD processes are often characterized by the deposition of particles on oxide surfaces.[13,22,23] These particles coalesce and ultimately form a closed layer when the amount of the deposited metal is sufficient. The equivalent thickness as a function of the number of ALD cycles is displayed up to 800 cycles in Figure 4a for depositions carried out at 120 and 50
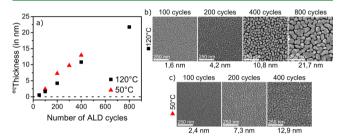

Figure 4. (a) Equivalent thickness of gold as a function of the number of ALD cycles performed on a silicon substrate (native oxide) for a substrate temperature of 50 and 120 °C. Saturating conditions were used for all depositions (i.e., a 15 s exposure time for both Me$_3$Au(PMe$_3$) and H$_2$ plasma). (b) Top SEM micrographs for PE-ALD films deposited at 120 °C. (c) Top SEM micrographs for PE-ALD films deposited at 50 °C.

°C. Ex situ SEM images of Au films deposited at 120 °C confirmed that this H$_2$ plasma process is governed by an island growth mode (Figure 4b). The ex situ SEM images of films deposited at 50 °C also revealed that island growth occurs at this temperature. At both substrate temperatures, the mean particle size clearly increased with the equivalent Au thickness and the general shape of the particles changed as well. Initially, the particle shapes were mainly circular, but with increasing film thickness, the particle shape became more irregular, attributed to the coalescence of particles with progressing deposition. When the thickness of the film was further increased, wormlike structures were observed for both cases which finally resulted in percolating films when sufficient material was deposited. Here, the threshold to form a percolating path on the surface and obtain measurable in-plane electronic conductivity was found to be different for both deposition temperatures. At 50 °C, percolating films were obtained at a thickness of 12.9 nm (a resistivity value of 16.5 ± 0.8 $\mu\Omega$ cm could be measured) while at 120 °C, even at a thickness of 21.7 nm, a percolating path was not yet obtained. As will be detailed in the following section, even thicker layers were necessary to form a percolating path on the surface. This shows that the temperature can have an impact on the surface mechanisms dictating the nucleation behavior for this process.

A final characteristic that was evaluated for the developed Au ALD process was the conformality of deposition on arrays of silicon micropillars. The silicon micropillars had a length of 50

μm, a width of 2 μm, and a center-to-center spacing of 4 μm, yielding an equivalent aspect ratio (EAR) of 10. The EAR is derived from Monte Carlo simulations and is defined as the aspect ratio of a hypothetical cylindrical hole that would require the same reactant exposure to achieve a conformal coating.[24] A 15 s exposure time was used for $Me_3Au(PMe_3)$ and 10 s for the H_2 plasma exposure during the depositions, performed at a substrate temperature of 120 °C. Using SEM and EDX measurements, the surface morphology and Au loading were investigated along the length of the pillars (Figure 5). The SEM images (Figure 5a) clearly show that Au was
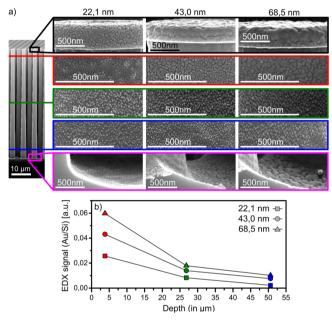

Figure 5. SEM images and EDX signal of gold films, deposited on silicon pillar structures (EAR = 10) at a substrate temperature of 120 °C. (a) SEM images for three film thicknesses (as measured on a planar silicon surface): 22.1 nm (800 cycles), 43.0 nm (1600 cycles), and 68.5 nm (2400 cycles). (b) EDX signal ratio of the Au peak to the Si peak as a function of distance from the top of the pillar structure.

deposited on the entire substrate and also between the pillars on the bottom surface of the structure. Increasing the thickness of the deposited film resulted in larger particles and more irregular shapes, as expected from the SEM images on planar substrates in Figure 4b,c. The morphology of the gold layer changed from being wormlike at the top of the pillar to smaller rounded particles near the bottom, suggesting that the amount of deposited gold on the side walls decreased when going from the top of the pillar to the bottom. To evaluate the Au loading, EDX line scans were taken at the height at which the SEM images were taken, and the ratio of the Au signal to the Si signal is displayed in Figure 5b as a function of depth in the structure. The data confirms that less gold was present on the side walls deeper in the structure, in agreement with the SEM images. The most likely reason for the nonideal conformality is a too low H_2 plasma exposure. Plasma radicals are known to recombine because of surface collisions, thus limiting the conformality,[25,26] in particular, during metal ALD due to the larger recombination rates on metallic surfaces.[27] Note that the SEM images visualizing the bottom of the structure and between the pillars revealed wormlike features. This points to a higher Au loading on the area between the pillars than on the bottom region of the pillars' side walls. This can be explained

by the fact that the bottom of the structure was in direct line of sight to the plasma, meaning that those surfaces received a larger direct flux of H radicals than the adjacent walls. Though this "bottom effect" is often predicted by simulation models,[24] the results presented here provide one of the few experimental examples. Overall, these initial depositions show that it is possible to deposit gold films on 3D structures.

3.2. Physical Properties and Film Composition. XRD measurements were performed on the deposited Au films to confirm their metallic nature. The obtained XRD patterns for films deposited at 120 and 50 °C are displayed in Figure 6a,b.
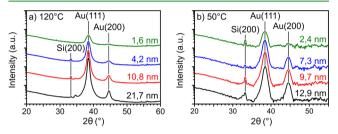

Figure 6. XRD patterns for deposited gold films with an equivalent thickness between 1.6 and 21.7 nm. For all thicknesses, the Au(111) and Au(200) peaks are visible at 38.5° and 44.6°, respectively. The patterns were given an offset for clarity. (a) Films deposited at 120 °C and (b) films deposited at 50 °C.

The patterns showed that the films were polycrystalline because of the presence of diffraction peaks from the Au(111) and Au(200) planes of the cubic gold crystals. These diffraction patterns hint that the as-deposited Au films are polycrystalline for all deposited thicknesses and for the full range of the ALD temperature window.

The composition of the deposited gold films was investigated using XPS measurements. Figure 7 shows the
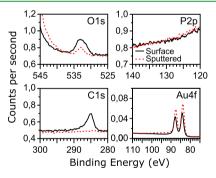

Figure 7. XPS spectra for a PE-ALD-grown Au film deposited at 120 °C with an equivalent thickness of 21.7 nm. The signals are given for the as-deposited film after removing surface contamination by Ar sputtering. The Si 2p peak (99.4 eV) is not visible.

Au 4f, C 1s, O 1s, and P 2p spectra. The sample was a silicon substrate on which 800 ALD cycles were performed at 120 °C, yielding an equivalent gold thickness of 21.7 nm. This deposition temperature, at the higher limit of the temperature window, was purposefully selected for comparison with the previously reported gold ALD processes.[13,14] XPS spectra were measured on the as-deposited film (contaminated by air exposure) and after removing the contaminating top layer by Ar sputtering in the XPS chamber. The surface composition for both cases is given in Table 1. This shows that the grown films are pure gold films with <1 at. % carbon and oxygen impurities

Table 1. XPS Concentrations of Au, C, O, and P of a PE-ALD-Grown Au Film Deposited at 120 °C with an Equivalent Thickness of 21.7 nm[a]

	Au 4f (at. %)	C 1s (at. %)	O 1s (at. %)	P 2p (at. %)
surface	95.5	3.4	1.1	<0.1
sputtered	99.4	0.3	0.3	<0.1

[a]The atomic concentration is given for the surface of the (air-exposed) as-deposited film on the first row. On the second row the atomic concentration is given after removing the surface contamination from the sample by Ar sputtering in the XPS chamber.

Figure 8. SEM images of a gold film (2400 cycles) deposited at 120 °C on a Si substrate with native oxide. The measured equivalent thickness via XRF is 65.6 nm. (a) Top SEM image showing a percolating film with the presence of voids and (b) cross-sectional SEM image on a cleaved edge of the Si substrate.

and no phosphorous (below the detection limit, <0.1 at. %) present in the film, values that are clearly lower than those obtained with the previous processes (Griffiths, Pallister, Mandia, and Barry reported 6.7 at. % carbon and 1.8 at. % oxygen impurities in their films deposited at 120 °C, and Mäkelä, Hatanpää, Mizohata, Räisänen, Ritala, and Leskelä reported 2.9 at. % oxygen, 0.9 at. % hydrogen, 0.2 at. % carbon, and 0.2 at. % nitrogen impurities in their films deposited at 180 °C).[13,14] The lack of phosphorous is a good indication that the P(CH₃)₃ ligands are effectively removed during the ALD surface reactions. After removal of the top layer of the film by argon sputtering, an O 1s peak remained with a binding energy of 832.8 eV, which corresponded to SiO₂. Therefore, the likely origin of the O 1s signal was the SiO₂ layer of the substrate. Alternatively, it is possible that minor oxygen contamination in the gold film originated from the glass tube of the plasma column, which may have been slightly etched during the H₂ plasma.[28] The SEM image of the 21.7 nm thick gold film (Figure 4b) indicates that the film is not a closed layer, and therefore a silicon peak (99.4 eV) was expected, but a clear silicon 2p peak is missing. Because the information depth of XPS is limited to 5−10 nm, the gold film was most likely blocking the silicon substrate from the detector's line of sight. The Au 4f₇/₂ peak is located at 84.1 eV, close to the expected value of 84.0 eV, indicating gold in the metallic state. Furthermore, the Au 4f region had spin−orbit peaks that were separated in energy by the expected value of 3.7 eV.

Although the deposited films had very few impurities and were crystalline, films grown at 120 °C are not fully closed films at a thickness of 21.7 nm, as indicated by the SEM image in Figure 4b. The series of SEM images reveals the evolution from isolated circular Au nanoparticles to larger coalesced wormlike structures. However, the latter does not form a conductive path on the surface. In order to measure the resistivity of the deposited gold films, a thicker film with an equivalent thickness of 65.6 nm was deposited at 120 °C on a silicon substrate and four-point probe resistance measurements were performed. For this film, a resistivity value of 5.9 ± 0.3 $\mu\Omega$ cm was obtained. This value is a factor of 2.4 larger than the bulk value of gold (2.44 $\mu\Omega$ cm) and comparable to the resistivity value recently obtained for gold films grown by ALD using the Me₂Au(S₂CNEt₂) precursor (4.6−16 $\mu\Omega$ cm).[14] From the top SEM image of the gold film (Figure 8a), it is clear that a percolating film was grown, but there seem to be voids present in the film. Figure 8b shows a cross-sectional SEM image on a cleaved edge of the Si substrate, allowing for a visual estimation of the film thickness. The physical thickness varied between 62.0 and 78.1 nm, which is in reasonable agreement with the equivalent thickness of 65.6 nm (obtained from XRF). Both images show that the deposited films were very rough, with an RMS roughness value of 6.5 nm obtained
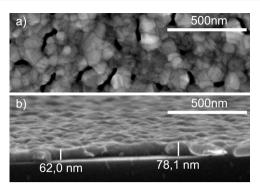
from AFM measurements (Figure S2). The reason for the higher resistivity, compared to the bulk value of gold, is probably the very rough surface morphology and the presence of holes in the film, lengthening the electrical path.

3.3. Surface Morphology and Raman Spectroscopy. Because of the rough, void-filled nature of the gold films, we speculated that these would be effective SERS substrates. LSPR are needed for a substrate to exhibit SERS properties, and creating very narrow (nanometer-sized) gaps between regular nanostructures made out of Au or Ag is a common approach to create LSPR hotspots on a substrate. The enhancement factor (EF) of the SERS signal scales with the inverse of the squared gap-size (d_g): EF $\approx 1/d_g^2$.[29] The gaps between the PE-ALD deposited gold nanoparticles are of nanometer size, indicating that these can act as LSPR hotspots. To verify this, free-space Raman spectroscopy measurements were performed on a series of four PE-ALD samples deposited at 120 °C, with different gold loadings (Figure 4b). The obtained Raman spectra and the calculated pump to Stokes conversion efficiencies (P_s/P_p) are shown in Figure 9. The pump to Stokes conversion efficiencies were based on the 1339 cm⁻¹ Raman mode, using the method described by Peyskens, Wuytens, Raza, Van Dorpe, and Baets.[30] The thinnest sample (1.6 nm) did not show a decent Raman spectrum of the pNTP molecule while the other samples clearly did.[31] A stronger Raman signal was observed with increasing equivalent thickness of the PE-ALD gold film. This can also be seen from the trend for the P_s/P_p conversion efficiencies, with the largest increase (×56) between the two thinnest samples (1.6 and 4.2 nm).

To understand why a stronger Raman signal is measured for the higher gold loadings, it is necessary to determine the surface morphology of the measured samples. Top view SEM images can provide information about the mean particle diameter, gap size, and coverage. SEM images were acquired after the Raman measurement for each sample (Figure 10I) and compared to the SEM images of the as-deposited samples (Figure 4b and insets in Figure 10I). This was done to see if the deposited gold nanoparticles remained stable under the processing steps that were needed to bind the pNTP molecules to the surface and the actual Raman measurements. It is easy to see that the two thinnest samples (a and b) did not retain their morphology. Instead, the gold nanoparticles agglomerated into irregular clusters, leaving large gaps between the formed clusters. The other two samples seemed to be stable because no agglomerates of particles appeared. The final SEM images
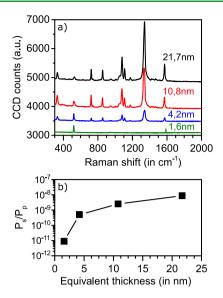
Figure 9. (a) Free-space Raman spectroscopy measurements on gold films for different equivalent thicknesses, deposited at 120 °C. The observed SERS spectra originate from pNTP molecules bound to the surface. The spectra were given an offset for clarity. (b) Calculated pump to Stokes conversion efficiency (P_s/P_p), based on the 1339 cm^{-1} Raman mode of pNTP, as a function of the equivalent thickness of the gold film. Note that the data points were not corrected for the number of adsorbed pNTP molecules because the estimated amount was found to be similar for all samples (see the Supporting Information).

were used to determine the mean particle diameter and gap size. This was done by manually analyzing a small section of the SEM images (300 × 300 nm). The obtained values are tabulated with their standard deviation in Table 2. These values indicate that the mean particle diameter increased with increasing gold loading, and a moderate increase was seen for the gap size.

The SEM images give a top-down view of the surface and do not contain information about the height of the particles. Ex situ GISAXS measurements were performed on the samples to determine the mean particle height. The obtained 2D scattering patterns can be seen in the Supporting Information (Figure S3). Modulations on the main scattering peak, along the q_z direction, contain information about the mean particle height. A line profile through the maximum of the scattering peak and along the q_z direction was extracted from each 2D pattern. The resulting profiles, together with their corresponding simulated line profiles, are displayed in Figure 10II. The expected q_z position of the scattering maximum (Yoneda peak) depends on the composition of the measured surface and is marked on the line profiles for a silicon and a gold surface.[32−34] The observed Yoneda peak started close to the expected value for a silicon surface with low gold loading (on sample a) and progressed with increasing gold loading toward the expected value for a pure gold surface. The particle height can be estimated using the relation $H_p = 2\pi\Delta q_z - 1$, where Δq_z is the distance between the adjacent maxima or minima on the line profile. The distance between the maxima/minima of the line profile decreased with increasing gold loading, which indicates an increase in particle height for the samples with a higher gold loading. The line profile of sample (d) shows that the deposited gold layer was very rough because only one maximum can be clearly distinguished in the line profile. For

samples (a), (b), and (c), the particle height was determined from the final input parameters used for the simulation (Table 2). The shape of the gold nanoparticles can be expected to resemble oblate spheroids because the height of the particles is smaller than the particle diameter. The GISAXS pattern of the sample (d) was not simulated because of the wormlike shapes of the gold nanoparticles. An estimation for the particle height for the sample (d) was obtained, by analyzing the difference in the maxima's position for the line profiles of samples (c) and (d).

Figure 10III depicts the mean gap between particles (and particle ensembles) for each sample. The particle gaps on sample (a) exhibited two length scales, the distance between particle clusters and the distance between individual particles in these clusters. Although the individual particles had very small gaps between them, it does not seem to benefit the Raman signal. The gaps are either too small or the particles are merged at their boundaries and do not contribute to the Raman signal. This leaves interactions between the clusters which are clearly not sufficient to obtain a decent enhancement. For sample (b), the mean gap size decreases slightly. However, this cannot explain the large increase (×56) for the Raman signal compared to sample (a). The average particle is larger, which can be one factor that plays a role in the higher efficiency, as a size-dependent effect of the gold nanoparticles cannot be excluded.[35] This could mean that the gold nanoparticles on sample (a) are too small to exhibit a decent SERS signal. However, the different morphologies of both samples most likely play a larger role. For sample (a), the particles have agglomerated and most likely the particles in the clusters are merged, losing the very small particle gap. The nanoparticles on sample (b) have also agglomerated. However, in this case, the boundaries between particles are better defined. This means that on this sample, the small gaps between the particles are accessible for the pNTP molecules and thus can contribute to the SERS signal.

Another possible cause for the difference in the obtained SERS signal could be a difference in the number of adsorbed, and thus measured, pNTP molecules on each sample. To investigate this, we estimated the number of measured pNTP molecules on each sample based on an estimate of the accessible gold surface area and the reported adsorption density for pNTP on gold (see the Supporting Information).[36] We found no significant difference in the estimated number of adsorbed pNTP molecules when comparing the four ALD samples. This suggests that a difference in the number of measured pNTP molecules cannot solely explain the observed differences in the SERS signal intensity.

For the two samples with the highest gold loadings, the mean gap size increased but the conversion efficiency also increased, while the increase in gap size is expected to decrease the SERS signal. However, for these samples, the coalescence of particles during the PE-ALD process starts to have a visible effect on the shape of the gold nanoparticles. The particle shape starts to change from spheroids to more irregular shapes (e.g., triangular, elongated spheroids, and rods). On sample (c), this results in the formation of particles that have straight edges on them. The gaps between particles start to have a structure that resembles a channel. Because of this, the LSPR hotspots do not originate from the interaction of neighboring rounded particles but between the straight edges of the formed channels. The straight edges of the channel will cause a more stable gap size, along the length of the formed channel,
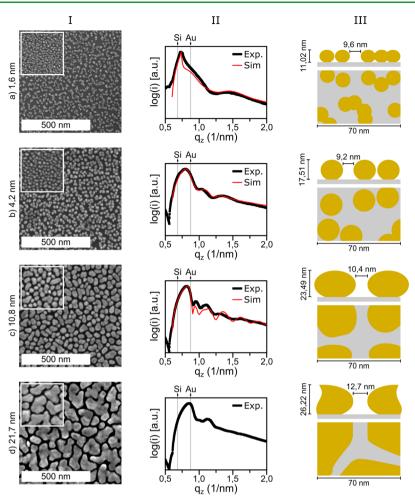
Figure 10. (I) SEM images of the samples after the Raman measurements, the inserts represent the sample before binding pNTP to the Au surface. (II) Vertical cut taken through the scattering maximum of the 2D GISAXS pattern and the simulation result of the cut. (III) Schematic depiction of the side view and the top view of the mean particle gap on each sample.

Table 2. Mean Particle Diameter (d_p), Gap-Size (d_g), Particle Height (H_p), and Pump to Stokes Conversion Efficiency (P_s/P_p) for Each Sample^a

sample	eq. thickness (in nm)	d_g (in nm)	d_p (in nm)	H_p (in nm)	P_s/P_p
(a)	1.6	9.6 ± 4.6	13.2 ± 2.9	11.02	9×10^{-12}
(b)	4.2	9.2 ± 4.1	19.9 ± 4.2	17.51	5×10^{-10}
(c)	10.8	10.4 ± 4.1	36.8 ± 9.2	23.49	2.5×10^{-9}
(d)	21.7	12.7 ± 4.5	54.4 ± 17	(26.22)	8.7×10^{-9}

^{a}The standard deviation for the mean particle diameter and gap size are reported next to the tabulated values.

compared to the gap between round particles. This increases the interaction volume where the LSPR hotspots occur, which counteracts the increase in the gap size. The largest gold loading is present on sample (d), and for this sample, the gold nanoparticles have coalesced even more than on sample (c). The resulting nanoparticles form very irregular wormlike shapes. As a result, it is possible for a channel to surround large portions of a particle. This starts to resemble the formation of "racetracks" on the surface, which can exhibit strong SERS enhancements because of their particular morphology. Such types of nanostructures fall in the class of "spoof plasmonics" in which the presence of gaps in a metal can cause LSPR hotspots.[37] Prokes, Glembocki, Cleveland, Caldwell, Foos, Niinistö, and Ritala demonstrated that this phenomenon can occur in PE-ALD deposited silver thin films because of the formation of "racetrack" structures in the silver thin film.[38]

Here, this particular morphology seems to cause a further increase in the Raman signal, despite the increase of the mean gap size compared to sample (c).

Although the optimal point of the PE-ALD-deposited gold films for SERS enhancement has not been determined, we believe this point must lie somewhere between the surface of sample (d) and a fully closed gold layer. Based on a reported study for sputtered silver films, the best Raman signal is expected at the percolation threshold of the film.[39] This could also be the case for the PE-ALD-deposited gold films.

To conclude, the strongest Raman signal is obtained for the sample with an equivalent thickness of 21.7 nm (sample d). Previously, a Stokes to pump conversion efficiency of 6×10^{-8} was reported for state-of-the-art gold nanodome substrates.[40] Correcting for a roughly three times higher accessible gold surface area for the ALD samples (meaning a three times

higher pNTP concentration), we can conclude that our best sample has a slightly more than one order of magnitude weaker conversion efficiency (factor 21). This is promising, given that there is still room for optimization of the Au ALD films. Although ALD layers have already been used to form protective coatings on SERS substrates and to design the gap of the slot on SiN waveguides for on-chip SERS applications,[41,42] this work shows that it is possible to create an effective SERS substrate using the reported PE-ALD process, without the need for lithography or a sequence of processing steps.

4. CONCLUSIONS

Growth of pure metallic gold films at the lowest reported temperature to date has been demonstrated with a PE-ALD process, using $Me_3Au(PMe_3)$ and H_2 plasma as the precursor and the reactant, respectively. The process exhibits saturation of the precursor and reactant half cycles on gold seed layers with a steady growth rate of 0.030 ± 0.002 nm per cycle. A similar steady growth rate is obtained on bare SiO_2 surfaces, after a sufficient number of cycles. Initially, the growth rate is lower because of nucleation, leading to islandlike growth and high film roughness, but percolating films are obtained when the films are sufficiently thick. A resistivity value of 5.9 ± 0.3 $\mu\Omega$ cm is obtained for the thickest films, close to the bulk resistivity value of gold (2.44 $\mu\Omega$ cm). The deposited films are pure gold with <1 at. % carbon and oxygen impurities in the film. The particular nanostructure of as-deposited films offers stable free-space Raman enhancement, slightly more than one order of magnitude lower than that of state-of-the-art solid-state substrates, but with room for further optimization. The SERS-active Au ALD substrates can be fabricated with relative ease without the need for complex-processing or lithography steps. Beyond SERS, nanoparticulate gold has very interesting and useful catalytic properties,[1−3] making the reported gold nanoparticle ALD process also highly relevant toward heterogeneous catalysis applications.

■ ASSOCIATED CONTENT

ⓢ Supporting Information

The Supporting Information is available free of charge on the ACS Publications website at DOI: 10.1021/acsami.9b10848.

> Equivalent thicknesses and [eq]GPC for depositions on native and thermal silicon oxide; AFM image of a 65.6 nm thick Au film on native silicon oxide; 2D GISAXS scattering images of ex situ gold films; cropped SEM image of an ALD Au sample, masks placed over the individual gold particles and border of the individual masks; and estimation procedure for the Au surface area and number of pNTP molecules (PDF)

■ AUTHOR INFORMATION

Corresponding Author

*E-mail: jolien.dendooven@ugent.be.

ORCID Ⓞ

Michiel Van Daele: 0000-0002-5452-8690
Matthias M. Minjauw: 0000-0003-3620-8949
Eduardo Solano: 0000-0002-2348-2271
Ranjith K. Ramachandran: 0000-0002-9423-219X
Christophe Detavernier: 0000-0001-7653-0858
Jolien Dendooven: 0000-0002-2385-3693

■ REFERENCES

(1) Daniel, M.-C.; Astruc, D. Gold Nanoparticles: Assembly, Supramolecular Chemistry, Quantum-Size-Related Properties, and Applications toward Biology, Catalysis, and Nanotechnology. *Chem. Rev.* **2004**, *104*, 293−346.

(2) Hashmi, A. S. K.; Hutchings, G. J. Gold Catalysis. *Angew. Chem., Int. Ed.* **2006**, *45*, 7896−7936.

(3) Zhang, Y.; Cui, X.; Shi, F.; Deng, Y. Nano-Gold Catalysis in Fine Chemical Synthesis. *Chem. Rev.* **2012**, *112*, 2467−2505.

(4) Freestone, I.; Meeks, N.; Sax, M.; Higgitt, C. The Lycurgus Cup — A Roman Nanotechnology. *Gold Bull.* **2007**, *40*, 270−277.

(5) Willets, K. A.; Van Duyne, R. P. Localized Surface Plasmon Resonance Spectroscopy and Sensing. *Annu. Rev. Phys. Chem.* **2007**, *58*, 267−297.

(6) Mayer, K. M.; Hafner, J. H. Localized Surface Plasmon Resonance Sensors. *Chem. Rev.* **2011**, *111*, 3828−3857.

(7) Hampden-Smith, M. J.; Kodas, T. T. Chemical Vapor Deposition of Metals: Part 1. An Overview of CVD Processes. *Chem. Vap. Deposition* **1995**, *1*, 8−23.

(8) Bessonov, A. A.; Morozova, N. B.; Gelfond, N. V.; Semyannikov, P. P.; Trubin, S. V.; Shevtsov, Y. V.; Shubin, Y. V.; Igumenov, I. K. Dimethylgold(III) Carboxylates as new Precursors for Gold CVD. *Surf. Coat. Technol.* **2007**, *201*, 9099−9103.

(9) Messelhäuser, J.; Flint, E. B.; Suhr, H. Direct Writing of Gold Lines by Laser-Induced Chemical Vapor Deposition. *Appl. Phys. A: Solids Surf.* **1992**, *55*, 196−202.

(10) Baum, T. H.; Jones, C. R. Laser Chemical Vapor Deposition of Gold. *Appl. Phys. Lett.* **1985**, *47*, 538−540.

(11) Holl, M. M. B.; Seidler, P. F.; Kowalczyk, S. P.; McFeely, F. R. Surface Reactivity of Alkylgold(I) Complexes: Substrate-Selective Chemical Vapor Deposition of Gold from $RAuP(CH_3)_3$ (R = CH_2CH_3, CH_3) at Remarkably Low Temperatures. *Inorg. Chem.* **1994**, *33*, 510−517.

(12) Mäkelä, M.; Hatanpää, T.; Ritala, M.; Leskelä, M.; Mizohata, K.; Meinander, K.; Räisänen, J. Potential Gold(I) Precursors Evaluated for Atomic Layer Deposition. *J. Vac. Sci. Technol., A* **2017**, *35*, 01B112.

(13) Griffiths, M. B. E.; Pallister, P. J.; Mandia, D. J.; Barry, S. T. Atomic Layer Deposition of Gold Metal. *Chem. Mater.* **2016**, *28*, 44−46.

(14) Mäkelä, M.; Hatanpää, T.; Mizohata, K.; Räisänen, J.; Ritala, M.; Leskelä, M. Thermal Atomic Layer Deposition of Continuous and Highly Conducting Gold Thin Films. *Chem. Mater.* **2017**, *29*, 6130−6136.

(15) Gong, S.; Schwalb, W.; Wang, Y.; Chen, Y.; Tang, Y.; Si, J.; Shirinzadeh, B.; Cheng, W. A Wearable and Highly Sensitive Pressure Sensor with Ultrathin Gold Nanowires. *Nat. Commun.* **2014**, *5*, 3132.

(16) Fateixa, S.; Pinheiro, P. C.; Nogueira, H. I. S.; Trindade, T. Gold Loaded Textile Fibres as Substrates for SERS Detection. *J. Mol. Struct.* **2019**, *1185*, 333−340.

(17) Kim, J.-H.; Twaddle, K. M.; Hu, J.; Byun, H. Sunlight-Induced Synthesis of Various Gold Nanoparticles and Their Heterogeneous Catalytic Properties on a Paper-Based Substrate. *ACS Appl. Mater. Interfaces* **2014**, *6*, 11514−11522.

(18) Yu, Y.; Zeng, P.; Yang, C.; Gong, J.; Liang, R.; Ou, Q.; Zhang, S. Gold-Nanorod-Coated Capillaries for the SERS-Based Detection of Thiram. *ACS Appl. Nano Mater.* **2019**, *2*, 598−606.

(19) Kim, H.-M.; Uh, M.; Jeong, D. H.; Lee, H.-Y.; Park, J.-H.; Lee, S.-K. Localized Surface Plasmon Resonance Biosensor using Nano-patterned Gold Particles on the Surface of an Optical Fiber. *Sens. Actuators, B* **2019**, *280*, 183−191.

(20) Levrau, E.; Van de Kerckhove, K.; Devloo-Casier, K.; Pulinthanathu Sree, S.; Martens, J. A.; Detavernier, C.; Dendooven, J. In Situ IR Spectroscopic Investigation of Alumina ALD on Porous Silica Films: Thermal versus Plasma-Enhanced ALD. *J. Phys. Chem. C* **2014**, *118*, 29854−29859.

(21) Portale, G.; Cavallo, D.; Alfonso, G. C.; Hermida-Merino, D.; van Drongelen, M.; Balzano, L.; Peters, G. W. M.; Goossens, J. G. P.; Bras, W. Polymer Crystallization Studies under Processing-Relevant Conditions at the SAXS/WAXS DUBBLE Beamline at the ESRF. *J. Appl. Crystallogr.* **2013**, *46*, 1681−1689.

(22) Dendooven, J.; et al. Independent Tuning of Size and Coverage of Supported Pt Nanoparticles using Atomic Layer Deposition. *Nat. Commun.* **2017**, *8*, 1074.

(23) Minjauw, M. M.; Solano, E.; Sree, S. P.; Asapu, R.; Van Daele, M.; Ramachandran, R. K.; Heremans, G.; Verbruggen, S. W.; Lenaerts, S.; Martens, J. A.; Detavernier, C.; Dendooven, J. Plasma-Enhanced Atomic Layer Deposition of Silver Using $Ag(fod)(PEt_3)$ and NH_3-Plasma. *Chem. Mater.* **2017**, *29*, 7114−7121.

(24) Cremers, V.; Puurunen, R. L.; Dendooven, J. Conformality in Atomic Layer Deposition: Current Status Overview of Analysis and Modelling. *Appl. Phys. Rev.* **2019**, *6*, 021302.

(25) Dendooven, J.; Deduytsche, D.; Musschoot, J.; Vanmeirhaeghe, R. L.; Detavernier, C. Conformality of Al_2O_3 and AlN Deposited by Plasma-Enhanced Atomic Layer Deposition. *J. Electrochem. Soc.* **2010**, *157*, G111−G116.

(26) Knoops, H. C. M.; Langereis, E.; van de Sanden, M. C. M.; Kessels, W. M. M. Conformality of Plasma-Assisted ALD: Physical Processes and Modeling. *J. Electrochem. Soc.* **2010**, *157*, G241−G249.

(27) Erkens, I. J. M.; Verheijen, M. A.; Knoops, H. C. M.; Keuning, W.; Roozeboom, F.; Kessels, W. M. M. Plasma-Assisted Atomic Layer Deposition of Conformal Pt Films in High Aspect Ratio Trenches. *J. Chem. Phys.* **2017**, *146*, 052818.

(28) Chang, R. P. H.; Chang, C. C.; Darack, S. Hydrogen Plasma Etching of Semiconductors and their Oxides. *J. Vac. Sci. Technol.* **1982**, *20*, 45−50.

(29) McMahon, J. M.; Li, S.; Ausman, L. K.; Schatz, G. C. Modeling the Effect of Small Gaps in Surface-Enhanced Raman Spectroscopy. *J. Phys. Chem. C* **2012**, *116*, 1627−1637.

(30) Peyskens, F.; Wuytens, P.; Raza, A.; Van Dorpe, P.; Baets, R. Waveguide Excitation and Collection of Surface-Enhanced Raman Scattering from a Single Plasmonic Antenna. *Nanophotonics* **2018**, *7*, 1299−1306.

(31) Wallace, G. Q.; Tabatabaei, M.; Lagugné-Labarthet, F. Towards Attomolar Detection using a Surface-Enhanced Raman Spectroscopy Platform Fabricated by Nanosphere Lithography. *Can. J. Chem.* **2014**, *92*, 1.

(32) Yoneda, Y. Anomalous Surface Reflection of X Rays. *Phys. Rev.* **1963**, *131*, 2010−2013.

(33) Holý, V.; Baumbach, T. Nonspecular X-ray Reflection from Rough Multilayers. *Phys. Rev. B: Condens. Matter Mater. Phys.* **1994**, *49*, 10668−10676.

(34) Schwartzkopf, M.; et al. From Atoms to Layers: in situ Gold Cluster Growth Kinetics during Sputter Deposition. *Nanoscale* **2013**, *5*, 5053−5062.

(35) Bell, S. E. J.; McCourt, M. R. SERS Enhancement by Aggregated Au Colloids: Effect of Particle Size. *Phys. Chem. Chem. Phys.* **2009**, *11*, 7455−7462.

(36) Wuytens, P. C.; Skirtach, A. G.; Baets, R. On-Chip Surface-Enhanced Raman Spectroscopy using Nanosphere-Lithography Patterned Antennas on Silicon Nitride Waveguides. *Opt. Express* **2017**, *25*, 12926−12934.

(37) Pendry, J. B.; Martín-Moreno, L.; Garcia-Vidal, F. J. Mimicking Surface Plasmons with Structured Surfaces. *Science* **2004**, *305*, 847−848.

(38) Prokes, S. M.; Glembocki, O. J.; Cleveland, E.; Caldwell, J. D.; Foos, E.; Niinistö, J.; Ritala, M. Spoof-like Plasmonic Behavior of Plasma Enhanced Atomic Layer Deposition Grown Ag Thin Films. *Appl. Phys. Lett.* **2012**, *100*, 053106.

(39) Santoro, G.; Yu, S.; Schwartzkopf, M.; Zhang, P.; Koyiloth Vayalil, S.; Risch, J. F. H.; Rübhausen, M. A.; Hernández, M.; Domingo, C.; Roth, S. V. Silver Substrates for Surface Enhanced Raman Scattering: Correlation between Nanostructure and Raman Scattering Enhancement. *Appl. Phys. Lett.* **2014**, *104*, 243107.

(40) Wuytens, P. C.; Subramanian, A. Z.; De Vos, W. H.; Skirtach, A. G.; Baets, R. Gold Nanodome-Patterned Microchips for Intra-cellular Surface-Enhanced Raman Spectroscopy. *Analyst* **2015**, *140*, 8080−8087.

(41) Formo, E. V.; Mahurin, S. M.; Dai, S. Robust SERS Substrates Generated by Coupling a Bottom-Up Approach and Atomic Layer Deposition. *ACS Appl. Mater. Interfaces* **2010**, *2*, 1987−1991.

(42) Raza, A.; Clemmen, S.; Wuytens, P.; Muneeb, M.; Van Daele, M.; Dendooven, J.; Detavernier, C.; Skirtach, A.; Baets, R. ALD Assisted Nanoplasmonic Slot Waveguide for On-Chip Enhanced Raman Spectroscopy. *APL Photonics* **2018**, *3*, 116105.